

Extended Measurement of the Cosmic-Ray Electron and Positron Spectrum from 11 GeV to 4.8 TeV with the Calorimetric Electron Telescope on the International Space Station

O. Adriani,^{1,2} Y. Akaike,^{3,4} K. Asano,⁵ Y. Asaoka,^{6,7,*} M.G. Bagliesi,^{8,9} E. Berti,^{1,2} G. Bigongiari,^{8,9}
W.R. Binns,¹⁰ S. Bonechi,^{8,9} M. Bongi,^{1,2} P. Brogi,^{8,9} J.H. Buckley,¹⁰ N. Cannady,¹¹ G. Castellini,¹²
C. Checchia,^{13,14} M.L. Cherry,¹¹ G. Collazuol,^{13,14} V. Di Felice,^{15,16} K. Ebisawa,¹⁷ H. Fuke,¹⁷ T.G. Guzik,¹¹
T. Hams,^{3,18} M. Hareyama,¹⁹ N. Hasebe,⁶ K. Hibino,²⁰ M. Ichimura,²¹ K. Ioka,²² W. Ishizaki,⁵ M.H. Israel,¹⁰
K. Kasahara,⁶ J. Kataoka,⁶ R. Kataoka,²³ Y. Katayose,²⁴ C. Kato,²⁵ N. Kawanaka,^{26,27} Y. Kawakubo,²⁸
K. Kohri,²⁹ H.S. Krawczynski,¹⁰ J.F. Krizmanic,^{18,3} T. Lomtadze,⁹ P. Maestro,^{8,9} P.S. Marrocchesi,^{8,9}
A.M. Messineo,^{30,9} J.W. Mitchell,⁴ S. Miyake,³¹ A.A. Moiseev,^{32,18} K. Mori,^{6,17} M. Mori,³³ N. Mori,²
H.M. Motz,³⁴ K. Munakata,²⁵ H. Murakami,⁶ S. Nakahira,³⁵ J. Nishimura,¹⁷ G.A. de Nolfo,³⁶ S. Okuno,²⁰
J.F. Ormes,³⁷ S. Ozawa,⁶ L. Pacini,^{1,12,2} F. Palma,^{15,16} P. Papini,² A.V. Penacchioni,^{8,38} B.F. Rauch,¹⁰
S.B. Ricciarini,^{12,2} K. Sakai,^{18,3} T. Sakamoto,²⁸ M. Sasaki,^{18,32} Y. Shimizu,²⁰ A. Shiomi,³⁹ R. Sparvoli,^{15,16}
P. Spillantini,¹ F. Stolzi,^{8,9} J.E. Suh,^{8,9} A. Sulaj,^{8,9} I. Takahashi,⁴⁰ M. Takayanagi,¹⁷ M. Takita,⁵
T. Tamura,²⁰ N. Tateyama,²⁰ T. Terasawa,³⁵ H. Tomida,¹⁷ S. Torii,^{6,7,41,†} Y. Tsunesada,⁴² Y. Uchihori,⁴³
S. Ueno,¹⁷ E. Vannuccini,² J.P. Wefel,¹¹ K. Yamaoka,⁴⁴ S. Yanagita,⁴⁵ A. Yoshida,²⁸ and K. Yoshida⁴⁶

(CALET Collaboration)

¹Department of Physics, University of Florence, Via Sansone, 1 - 50019 Sesto, Fiorentino, Italy

²INFN Sezione di Florence, Via Sansone, 1 - 50019 Sesto, Fiorentino, Italy

³Department of Physics, University of Maryland, Baltimore County,
1000 Hilltop Circle, Baltimore, MD 21250, USA

⁴Astroparticle Physics Laboratory, NASA/GSFC, Greenbelt, MD 20771, USA

⁵Institute for Cosmic Ray Research, The University of Tokyo,
5-1-5 Kashiwa-no-Ha, Kashiwa, Chiba 277-8582, Japan

⁶Research Institute for Science and Engineering,
Waseda University, 3-4-1 Okubo, Shinjuku, Tokyo 169-8555, Japan

⁷JEM Utilization Center, Human Spaceflight Technology Directorate,
Japan Aerospace Exploration Agency, 2-1-1 Sengen, Tsukuba, Ibaraki 305-8505, Japan

⁸Department of Physical Sciences, Earth and Environment,
University of Siena, via Roma 56, 53100 Siena, Italy

⁹INFN Sezione di Pisa, Polo Fibonacci, Largo B. Pontecorvo, 3 - 56127 Pisa, Italy

¹⁰Department of Physics, Washington University,
One Brookings Drive, St. Louis, MO 63130-4899, USA

¹¹Department of Physics and Astronomy, Louisiana State University,
202 Nicholson Hall, Baton Rouge, LA 70803, USA

¹²Institute of Applied Physics (IFAC), National Research Council (CNR),
Via Madonna del Piano, 10, 50019 Sesto, Fiorentino, Italy

¹³Department of Physics and Astronomy, University of Padova, Via Marzolo, 8, 35131 Padova, Italy

¹⁴INFN Sezione di Padova, Via Marzolo, 8, 35131 Padova, Italy

¹⁵University of Rome "Tor Vergata", Via della Ricerca Scientifica 1, 00133 Rome, Italy

¹⁶INFN Sezione di Rome "Tor Vergata", Via della Ricerca Scientifica 1, 00133 Rome, Italy

¹⁷Institute of Space and Astronautical Science, Japan Aerospace Exploration Agency,
3-1-1 Yoshinodai, Chuo, Sagami, Kanagawa 252-5210, Japan

¹⁸CRESST and Astroparticle Physics Laboratory NASA/GSFC, Greenbelt, MD 20771, USA

¹⁹St. Marianna University School of Medicine, 2-16-1,
Sugao, Miyamae-ku, Kawasaki, Kanagawa 216-8511, Japan

²⁰Kanagawa University, 3-27-1 Rokkakubashi, Kanagawa, Yokohama, Kanagawa 221-8686, Japan

²¹Faculty of Science and Technology, Graduate School of Science and Technology,
Hirosaki University, 3, Bunkyo, Hirosaki, Aomori 036-8561, Japan

²²Yukawa Institute for Theoretical Physics, Kyoto University,
Kitashirakawa Oiwakecho, Sakyo, Kyoto 606-8502, Japan

²³National Institute of Polar Research, 10-3, Midori-cho, Tachikawa, Tokyo 190-8518, Japan

²⁴Faculty of Engineering, Division of Intelligent Systems Engineering,
Yokohama National University, 79-5 Tokiwadai, Hodogaya, Yokohama 240-8501, Japan

²⁵Faculty of Science, Shinshu University, 3-1-1 Asahi, Matsumoto, Nagano 390-8621, Japan

²⁶Hakubi Center, Kyoto University, Yoshida Honmachi, Sakyo-ku, Kyoto, 606-8501, Japan

²⁷Department of Astronomy, Graduate School of Science, Kyoto University,
Kitashirakawa Oiwake-cho, Sakyo-ku, Kyoto, 606-8502, Japan

²⁸ *College of Science and Engineering, Department of Physics and Mathematics, Aoyama Gakuin University, 5-10-1 Fuchinobe, Chuo, Sagamihara, Kanagawa 252-5258, Japan*

²⁹ *Institute of Particle and Nuclear Studies, High Energy Accelerator Research Organization, 1-1 Oho, Tsukuba, Ibaraki, 305-0801, Japan*

³⁰ *University of Pisa, Polo Fibonacci, Largo B. Pontecorvo, 3 - 56127 Pisa, Italy*

³¹ *Department of Electrical and Electronic Systems Engineering, National Institute of Technology, Ibaraki College, 866 Nakane, Hitachinaka, Ibaraki 312-8508 Japan*

³² *Department of Astronomy, University of Maryland, College Park, Maryland 20742, USA*

³³ *Department of Physical Sciences, College of Science and Engineering, Ritsumeikan University, Shiga 525-8577, Japan*

³⁴ *International Center for Science and Engineering Programs, Waseda University, 3-4-1 Okubo, Shinjuku, Tokyo 169-8555, Japan*

³⁵ *RIKEN, 2-1 Hirosawa, Wako, Saitama 351-0198, Japan*

³⁶ *Heliospheric Physics Laboratory, NASA/GSFC, Greenbelt, MD 20771, USA*

³⁷ *Department of Physics and Astronomy, University of Denver, Physics Building, Room 211, 2112 East Wesley Ave., Denver, CO 80208-6900, USA*

³⁸ *ASI Science Data Center (ASDC), Via del Politecnico snc, 00133 Rome, Italy*

³⁹ *College of Industrial Technology, Nihon University, 1-2-1 Izumi, Narashino, Chiba 275-8575, Japan*

⁴⁰ *Kavli Institute for the Physics and Mathematics of the Universe, The University of Tokyo, 5-1-5 Kashiwanoha, Kashiwa, 277-8583, Japan*

⁴¹ *School of Advanced Science and Engineering, Waseda University, 3-4-1 Okubo, Shinjuku, Tokyo 169-8555, Japan*

⁴² *Division of Mathematics and Physics, Graduate School of Science,*

Osaka City University, 3-3-138 Sugimoto, Sumiyoshi, Osaka 558-8585, Japan

⁴³ *National Institutes for Quantum and Radiation Science and Technology, 4-9-1 Anagawa, Inage, Chiba 263-8555, JAPAN*

⁴⁴ *Nagoya University, Furo, Chikusa, Nagoya 464-8601, Japan*

⁴⁵ *College of Science, Ibaraki University, 2-1-1 Bunkyo, Mito, Ibaraki 310-8512, Japan*

⁴⁶ *Department of Electronic Information Systems, Shibaura Institute of Technology, 307 Fukasaku, Minuma, Saitama 337-8570, Japan*

(Dated: June 27, 2018)

Extended results on the cosmic-ray electron + positron spectrum from 11 GeV to 4.8 TeV are presented based on observations with the Calorimetric Electron Telescope (CALET) on the International Space Station utilizing the data up to November 2017. The analysis uses the full detector acceptance at high energies, approximately doubling the statistics compared to the previous result. CALET is an all-calorimetric instrument with a total thickness of $30 X_0$ at normal incidence and fine imaging capability, designed to achieve large proton rejection and excellent energy resolution well into the TeV energy region. The observed energy spectrum in the region below 1 TeV shows good agreement with Alpha Magnetic Spectrometer (AMS-02) data. In the energy region below ~ 300 GeV, CALET's spectral index is found to be consistent with the AMS-02, Fermi Large Area Telescope (Fermi-LAT), and DARK MATTER Particle Explorer (DAMPE), while from 300 to 600 GeV the spectrum is significantly softer than the spectra from the latter two experiments. The absolute flux of CALET is consistent with other experiments at around a few tens of GeV. However, it is lower than those of DAMPE and Fermi-LAT with the difference increasing up to several hundred GeV. The observed energy spectrum above ~ 1 TeV suggests a flux suppression consistent within the errors with the results of DAMPE, while CALET does not observe any significant evidence for a narrow spectral feature in the energy region around 1.4 TeV. Our measured all-electron flux, including statistical errors and a detailed breakdown of the systematic errors, is tabulated in the Supplemental Material in order to allow more refined spectral analyses based on our data.

PACS numbers: 96.50.sb,95.35.+d,95.85.Ry,98.70.Sa,29.40.Vj

INTRODUCTION

High-energy cosmic-ray electrons provide a unique probe of nearby cosmic accelerators. Electrons rapidly lose energy via inverse Compton scattering and synchrotron emission during propagation in the Galaxy. Since their diffusion distance above 1 TeV is less than 1 kpc, only a few potential TeV sources are expected in the vicinity of the Solar System. A precise measurement of the electron spectrum in the TeV region might reveal interesting spectral features to provide the first ex-

perimental evidence of the possible presence of a nearby cosmic-ray source [1, 2]. In addition, the prominent increase of the positron fraction over 10 GeV established by the Payload for Antimatter Matter Exploration and Light-nuclei Astrophysics (PAMELA) [3] and the Alpha Magnetic Spectrometer (AMS-02) [4] may require a primary source component for positrons in addition to the generally accepted secondary origin. Candidates for such primary sources range from astrophysical (pulsar) to exotic (dark matter). Since these primary sources emit electron-positron pairs, it is expected that the all-electron

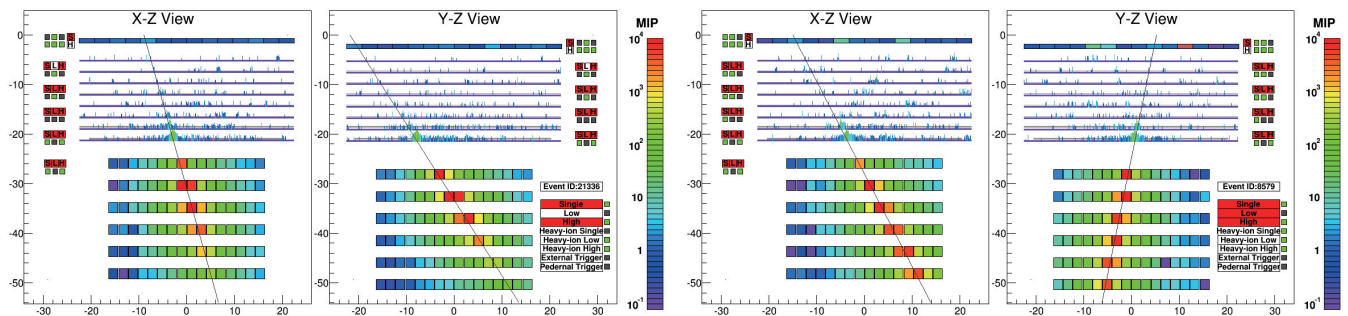


FIG. 1. Examples of TeV event candidates showing energy deposit in each detector channel in the $X - Z$ and $Y - Z$ views. (Left) An electron (or positron) candidate (reconstructed energy of 3.05 TeV and energy deposit sum of 2.89 TeV). (Right) A proton candidate (energy deposit sum of 2.89 TeV).

(electrons + positrons) spectrum would exhibit a spectral feature, near the highest energy range of the primary component.

The CALET Collaboration managing the CALorimetric Electron Telescope (CALET) [5], a space-based instrument optimized for the measurement of the all-electron spectrum, published its first result in the energy range from 10 GeV to 3 TeV [6]. Subsequently, the DArk Matter Particle Explorer (DAMPE) collaboration published their all-electron spectrum in the energy range from 25 GeV to 4.6 TeV [7].

In this Letter, we present an updated version of the CALET all-electron spectrum. Using 780 days of flight data from October 13, 2015 to November 30, 2017 and the full geometrical acceptance in the high-energy region, we have increased our statistics by a factor of ~ 2 compared to Ref. [6]. The energy range is also extended up to 4.75 TeV. Features of the spectrum measured by CALET are discussed, particularly in relation to the break reported by DAMPE at 0.9 TeV. The possible presence of a peak close to 1.4 TeV is tested with CALET data by using exactly the same energy binning as that of DAMPE. The systematic uncertainties are classified into several categories in order to allow for more sensitive interpretative studies using the CALET spectrum.

CALET INSTRUMENT

CALET employs a fully active calorimeter with 30 radiation-length thickness for particles at normal incidence. It consists of a charge detector (CHD), a 3 radiation-length thick imaging calorimeter (IMC) and a 27 radiation-length thick total absorption calorimeter (TASC), having a field of view of $\sim 45^\circ$ from zenith and a geometrical factor of $\sim 1040 \text{ cm}^2 \text{ sr}$ for high-energy electrons.

CHD, which identifies the charge of the incident particle, is comprised of a pair of plastic scintillator ho-

dosopes arranged in two orthogonal layers. IMC is a sampling calorimeter alternating thin layers of Tungsten absorber, optimized in thickness and position, with layers of scintillating fibers read-out individually. TASC is a tightly packed lead-tungstate (PbWO_4 ; PWO) hodoscope, capable of almost complete absorption of the TeV-electron showers. A more complete description of the instrument is given in the Supplemental Material of Ref. [6].

Figure 1 shows a 3.05 TeV-electron candidate and a proton candidate with comparable energy deposit (2.89 TeV) in the detector. Compared to hadron showers which have significant leakage, the containment of the electromagnetic shower creates a difference in shower shape especially in the bottom part of TASC, allowing for an accurate electron identification in the presence of a large hadron background. Together with the precision energy measurements from total absorption of electromagnetic showers, it is possible to derive the electron spectrum well into the TeV region with a straightforward and reliable analysis.

The instrument was launched on August 19, 2015 and emplaced on the Japanese Experiment Module-Exposed Facility on the International Space Station with an expected mission duration of five years (or more). Scientific observations [8] were started on October 13, 2015, and smooth and continuous operations have taken place since then.

DATA ANALYSIS

We have analyzed 780 days of flight data collected with a high-energy shower trigger [8]. Total live time in this period was 15,811 hours, corresponding to a live time fraction of 84%. The analysis was extended to use the full detector acceptance at higher energies as explained further down, otherwise it was done following the standard analysis procedure described in Ref. [6].

A Monte Carlo (MC) program was used to simulate physics processes and detector response based on the simulation package EPICS [9, 10] (EPICS9.20 / Cosmos8.00). Using MC event samples of electrons and protons, event selection and event reconstruction efficiencies, energy correction factor, and background contamination were derived. An independent analysis based on Geant4 [11] was performed, and small differences between the MC models are included in the systematic uncertainties. The detector model used in the Geant4 simulation is almost identical to the CALET computer aided design model. The Geant4 simulation employs the hadronic interaction models FTFP_BERT as the physics list, while DPMJET3 [12] is chosen as the hadronic interaction model in the EPICS simulation.

While excellent energy resolution inside the TeV region is one of the most important features of a thick calorimeter instrument like CALET or DAMPE, calibration errors must be carefully assessed and taken into account in the estimation of the actual energy resolution. Our energy calibration [13] includes the evaluation of the conversion factors between ADC units and energy deposits, ensuring linearity over each gain range (TASC has four gain ranges for each channel), and provides a seamless transition between neighboring gain ranges. Temporal gain variations occurring during long time observations are also corrected for in the calibration procedure [6]. The errors at each calibration step, such as the correction of position and temperature dependence, consistency between energy deposit peaks of noninteracting protons and helium, linear fit error of each gain range, and gain ratio measurements, as well as slope extrapolation, are included in the estimation of the energy resolution. As a result, a very high resolution of 2% or better is achieved above 20 GeV [13]. It should be noted that even with such a detailed calibration, the determining factor for the energy resolution is the calibration uncertainty, as the intrinsic resolution of CALET is $\sim 1\%$ as for DAMPE [14]. Intrinsic resolution refers to the detector's capability by design, taking advantage of the thick, fully-active total absorption calorimeter. Also important is the fact that the calibration error in the lower gain ranges is crucial for the spectrum measurements in the TeV range.

We use the ‘‘electromagnetic shower tracking’’ algorithm [15] to reconstruct the shower axis of each event, taking advantage of the electromagnetic shower shape and IMC design concept. As input for the electron identification, well-reconstructed and well-contained single-charged events are preselected by (1) an off-line trigger confirmation, (2) a geometrical condition, (3) a track quality cut to ensure reconstruction accuracy, (4) a charge selection using CHD, (5) a longitudinal shower development and (6) a lateral shower containment consistent with those expected for electromagnetic cascades. The geometrical condition in our analysis is divided into four categories (A, B, C, D), depending on which de-

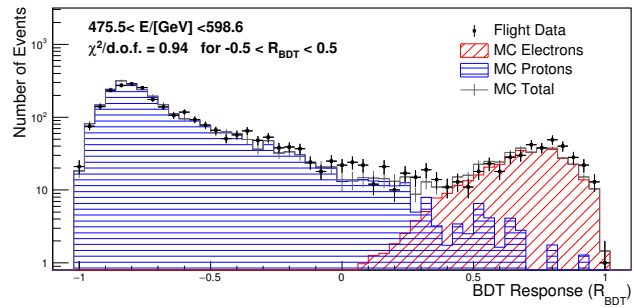


FIG. 2. An example of BDT response distributions in the 476 $< E < 599$ GeV bin including all acceptance conditions A, B, C and D. The BDT response distributions for the TeV region are shown in Fig. 2 of the Supplemental Material [16].

tor components are penetrated by the shower axis, explained in detail in Fig. 1 of the Supplemental Material [16] and its caption. In brief, A+B are fully contained events, while category C adds events incident from the IMC sides, and D adds events exiting through the sides of TASC. For events not crossing the CHD, we use the energy deposit of the first hit IMC layer to determine their charge.

The energy of incident electrons is reconstructed using the energy correction function, which converts the energy deposit information of TASC and IMC into primary energy for each geometrical condition. In order to identify electrons and to study systematic uncertainties in the electron identification, we applied two methods: a simple two parameter cut and a multivariate analysis based on boosted decision trees (BDTs). The details concerning these methods are explained in the Supplemental Material of Ref. [6].

Calculation of event selection efficiencies, BDT training, and estimation of proton background contamination are carried out separately for each geometrical condition, and combined in the end to obtain the final spectrum. Considering the fact that the lower energy region is dominated by systematics in our analysis and therefore more statistics would not significantly improve the precision of our data, the acceptance conditions C and D are only included in the higher energy region above 475 GeV. An example of a BDT response distribution including all acceptance conditions is shown in Fig. 2. In the final electron sample, the resultant contamination ratios of protons are $\sim 5\%$ up to 1 TeV, and 10%–20% in the 1–4.8 TeV region, while keeping a constant high efficiency of 80% for electrons. The number of electron candidates in the highest energy bin is seven.

The absolute energy scale was calibrated and shifted by +3.5% [6] as a result of a study of the geomagnetic cutoff energy [17]. Since the full dynamic range calibration [13] was carried out with a scale-free method, its

validity holds regardless of the absolute scale uncertainty.

SYSTEMATIC UNCERTAINTIES

As discussed in detail in Ref. [6] and its Supplemental Material, systematic uncertainties in our flux measurements can be divided into three categories, i.e., energy scale uncertainty, absolute normalization, and energy dependent uncertainties. As per the energy dependent systematics, we have identified the following contributions: trigger efficiency (below 30 GeV), BDT stability, tracking, charge identification, electron identification, and MC model dependence.

BDT stability is evaluated from the stability of the resultant flux for 100 independent training samples and for BDT cut efficiency variation from 70% to 90% in 1% steps for each corresponding test sample. Upper and lower panels of Fig. 2 in the Supplemental Material [16] show an example for the stability of the BDT analysis in the $949 < E < 1194$ GeV bin and its energy dependence, respectively, where good stability over a wide range of efficiency factors and number of training samples is demonstrated. Dependence on tracking, charge identification, electron identification and MC model is estimated by using the difference of the resultant flux between representative algorithms or methods, i.e., electromagnetic shower tracking vs combinatorial Kalman filter tracking [18] algorithms, CHD vs IMC charge identification methods, simple two parameter cut vs BDT cut, and the use of EPICS vs Geant4, respectively. The obtained energy dependence of the relative flux difference in each case is fitted with a suitable log-polynomial function to mitigate statistical fluctuations, as shown in Fig. 3 of the Supplemental Material [16]. Systematic effects up to a few percent are seen in the energy range below the TeV region. Statistical fluctuations are the most important limiting factor for estimating systematic errors in the TeV region, as indicated by the changes in the energy dependence of the MC model comparison from the previous publication [6]. By adding a factor of two more statistics in the highest energy region, the deviation in the 2–3 TeV bin changed significantly from the previous estimate, though by a smaller extent than the statistical error on the flux.

Since other selections, such as the track quality cut and shower concentration cuts, did not have a significant energy dependence, they were treated as uncertainties in the absolute normalization. Their contribution to the uncertainty in the absolute normalization was determined to be a very small part of the total. The total uncertainty in the absolute normalization was estimated to be 3.2%. A detailed breakdown of this uncertainty is given in the Supplemental Material of Ref. [6]. The high-energy trigger efficiency was verified by using data obtained with the low-energy trigger (1 GeV threshold) in the low rigidity

cutoff region below 6 GV. By comparing the flux with and without off-line trigger confirmation, the systematic uncertainty from trigger efficiency is estimated to be 2.4% below 30 GeV, mainly limited by the available low-energy triggered data, and is negligible above this energy. The resultant flux for each of the acceptance conditions used in this analysis is consistent within the statistical uncertainty, indicating that there are no significant systematic deviations among the acceptance conditions.

ELECTRON + POSITRON SPECTRUM

Figure 3 shows the extended electron and positron spectrum obtained with CALET using the same energy binning as in our previous publication, except for adding one extra bin at the high-energy end. The error bars along horizontal and vertical axes indicate bin width and statistical errors, respectively. The gray band is representative of the quadratic sum of statistical and systematic errors, using the same definition as the one given in Ref. [6]. Systematic errors include errors in the absolute normalization and energy dependent ones, except for the energy scale uncertainty. The energy dependent errors include those obtained from BDT stability, trigger efficiency in the low-energy region, tracking dependence, dependence on charge and electron identification methods and MC model dependence. In more refined interpretation studies, the latter four contributions could be treated as nuisance parameters while the first two components must be added in quadrature to the statistical errors. Conservatively, all of them are included in the total error estimate in Fig. 3. The measured all-electron flux including statistical errors and a detailed breakdown of the systematic errors into their components is tabulated in Table 1 of the Supplemental Material [16].

Comparing with other recent experiments [AMS-02, Fermi Large Area Telescope (Fermi-LAT) and DAMPE], our spectrum shows good agreement with AMS-02 data below 1 TeV. In the energy region from 40 to 300 GeV, the power-law index of CALET's spectrum is found to be -3.12 ± 0.02 , which is consistent with other experiments within errors. However, the spectrum is considerably softer from 300 to 600 GeV than the spectra measured by DAMPE and Fermi-LAT. The CALET results exhibit a lower flux than those of DAMPE and Fermi-LAT from 300 GeV up to near 1 TeV. In this region, a difference is noticeable between two groups of measurements with internal consistency within each group: CALET and AMS-02 vs Fermi-LAT and DAMPE, indicating the presence of unknown systematic effects.

In Fig. 4 we have adopted exactly the same energy binning as DAMPE to show our spectrum. The tabulated flux for this energy binning with a detailed breakdown of systematics is also shown in Table 2 of the Supplemental Material [16]. To check if the CALET spectrum

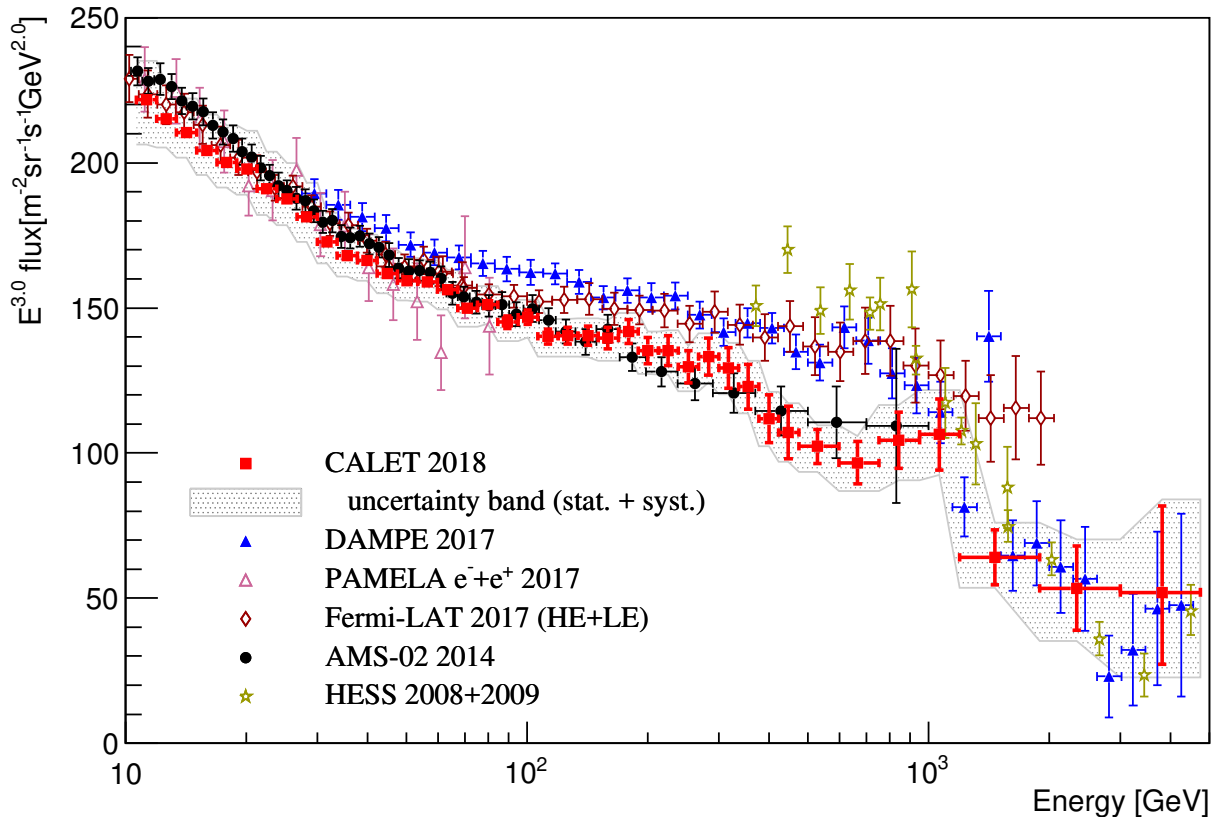


FIG. 3. Cosmic-ray all-electron spectrum measured by CALET from 10.6 GeV to 4.75 TeV using the same energy binning as in our previous publication [6], where the gray band indicates the quadratic sum of statistical and systematic errors (not including the uncertainty on the energy scale). Also plotted are direct measurements in space [7, 19–21] and from ground-based experiments [22, 23].

is consistent with a possible break at 0.9 TeV, as suggested by DAMPE’s observations, we fit our spectrum with a smoothly broken power-law model [7] in the energy range from 55 GeV to 2.63 TeV, while fixing the break energy at 914 GeV. A broken power law steepening from -3.15 ± 0.02 to -3.81 ± 0.32 fits our data well, with $\chi^2 = 17.0$ and number of degrees of freedom (NDF) equal to 25; this result is consistent with DAMPE regarding the spectral index change of 0.7 ± 0.3 . However, a single power-law fit over the same energy range gives an index -3.17 ± 0.02 with $\chi^2/\text{NDF} = 26.5/26$, not a significantly poorer goodness of fit than obtained with the broken power law. The fitting results are shown in Fig. 5 of the Supplemental Material [16], including a fit with an exponentially cutoff power law [20].

On the other hand, the flux in the 1.4 TeV bin of DAMPE’s spectrum, which might imply a peak structure, is not compatible with CALET results at a level of 4σ significance, including the systematic errors from both experiments. Since a sharp peak in a single bin

could be an artifact due to binning effects, we have studied this kind of effect as shown in Fig. 6 of the Supplemental Material [16] and explained in its caption. The result of this study excludes with good significance the hypothesis of the presence of a peaklike structure in our data. Furthermore, bin-to-bin migration and related effects are found to be negligible when compared with our estimated systematic uncertainties.

In conclusion, we extended our previous result [6] on the CALET all-electron spectrum both in energy (to 4.8 TeV) and in acceptance, with an approximate increase by a factor of 2 of the statistics in the higher energy region. The data in the TeV region show a suppression of the flux compatible with the DAMPE results. However, the accuracy of the break’s sharpness and position, and of the spectral shape above 1 TeV, will improve by better statistics and a further reduction of the systematic errors based on the analysis of additional flight data during the ongoing five-year (or more) observation. By specifying the breakdown of systematic uncertainties, our extended

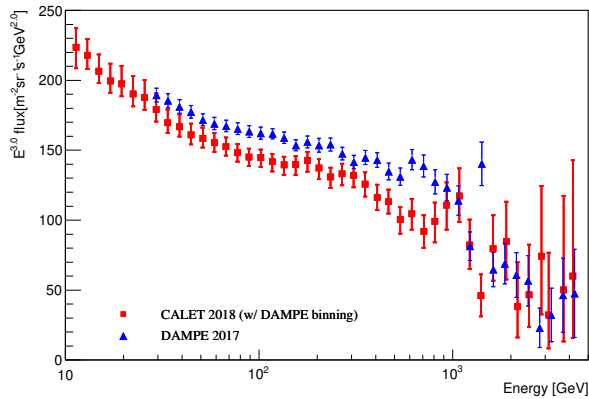


FIG. 4. Cosmic-ray all-electron spectrum measured by CALET from 10.6 GeV to 4.57 TeV using the same energy binning as DAMPE’s result [7] and compared with it. The error bars indicate the quadratic sum of statistical and systematic errors (not including the uncertainty on the energy scale).

all-electron spectrum together with the AMS-02 positron flux measurement [24] provides essential information to investigate spectral features in the framework of pulsars and/or dark matter inspired models.

ACKNOWLEDGMENTS

We gratefully acknowledge JAXA’s contributions to the development of CALET and to the operations on-board the International Space Station. We also wish to express our sincere gratitude to ASI and NASA for their support of the CALET project. This work was supported in part by a JSPS Grant-in-Aid for Scientific Research (S) (No. 26220708) and by the MEXT-Supported Program for the Strategic Research Foundation at Private Universities (2011-2015) (No. S1101021) at Waseda University. The CALET effort in the United States is supported by NASA through Grants No. NNX16AB99G,

No. NNX16AC02G, and No. NNX14ZDA001N-APRA-0075.

* yoichi.asaoka@aoni.waseda.jp

† torii.shoji@waseda.jp

- [1] J. Nishimura *et al.*, *Astrophys. J.* **238**, 394 (1980).
- [2] T. Kobayashi, Y. Komori, K. Yoshida, and J. Nishimura, *Astrophys. J.* **601**, 340 (2004).
- [3] O. Adriani *et al.*, *Nature* **458**, 607 (2009).
- [4] L. Accardo *et al.*, *Phys. Rev. Lett.* **113**, 121101 (2014).
- [5] S. Torii *et al.*, in *Proceeding of Science (ICRC2015)* 581 (2015).
- [6] O. Adriani *et al.*, *Phys. Rev. Lett.* **119**, 181101 (2017).
- [7] G. Ambrosi *et al.*, *Nature* **552**, 63 (2017).
- [8] Y. Asaoka, Y. Ozawa, S. Torii, *et al.*, *Astroparticle Physics* **100**, 29 (2018).
- [9] K. Kasahara, in *Proc. of 24th international cosmic ray conference (Rome, Italy)*, Vol. 1 (1995) p. 399.
- [10] K. Kasahara, EPICS, <http://cosmos.n.kanagawa-u.ac.jp/EPICSHome/>.
- [11] S. Agostinelli *et al.*, *Nucl. Instrum. Methods Phys. Res.* **A506**, 250 (2003).
- [12] S. Roesler, R. Engel, and J. Ranft, DPMJET, <http://sroesler.web.cern.ch/sroesler/dpmjet3.html>.
- [13] Y. Asaoka, Y. Akaike, Y. Komiya, R. Miyata, S. Torii, *et al.*, *Astroparticle Physics* **91**, 1 (2017).
- [14] J. Chang *et al.*, *Astroparticle Physics* **95**, 6 (2017).
- [15] Y. Akaike *et al.*, in *Proc. of 33rd international cosmic ray conference (ICRC2013)* 726 (2013).
- [16] See the Supplemental Material for supporting figures and the tabulated all-electron fluxes in two energy binnings.
- [17] M. Ackermann *et al.*, *Astroparticle Physics* **35**, 346 (2012).
- [18] P. Maestro, N. Mori, *et al.*, in *Proceedings of Science (ICRC2017)* 208 (2017).
- [19] O. Adriani *et al.*, *La Rivista del Nuovo Cimento* **40**, 473 (2017).
- [20] S. Abdollahi *et al.*, *Phys. Rev. D* **95**, 082007 (2017).
- [21] M. Aguilar *et al.*, *Phys. Rev. Lett.* **113**, 221102 (2014).
- [22] F. Aharonian *et al.*, *Phys. Rev. Lett.* **101**, 261104 (2008).
- [23] F. Aharonian *et al.*, *Astron Astrophys.* **508**, 561 (2009).
- [24] M. Aguilar *et al.*, *Phys. Rev. Lett.* **113**, 121102 (2014).

Extended Measurements of Cosmic-ray Electron and Positron Spectrum from 11 GeV to 4.8 TeV with the Calorimetric Electron Telescope on the International Space Station Supplemental online material.

Supplemental material concerning “Extended Measurements of Cosmic-ray Electron and Positron Spectrum from 11 GeV to 4.8 TeV with the Calorimetric Electron Telescope on the International Space Station.”

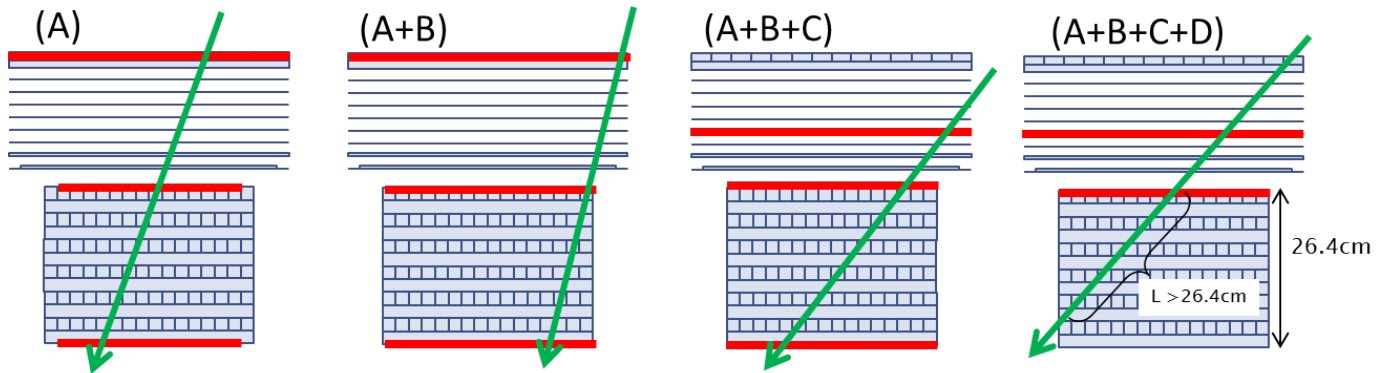


FIG. S1. Classification of four geometrical condition types. The red bars indicate the geometrical requirements for the particle trajectory at different detector layers. In each of the plots, the green arrow shows an example of a shower axis which is allowed by the extension of the geometrical condition. Geometrical condition A requires the shower axis to cross the TASC top and bottom layers except for a 2 cm outer margin, while in geometrical condition A+B the shower axis is allowed to cross the edge of TASC. In geometrical condition A+B+C, incidence from the side is allowed, but passage through the IMC 5th layer is required. Geometrical condition A+B+C+D does not require crossing of the TASC bottom layer, but it is required that the track length in TASC is greater than 26.4 cm. Each of A, B, C and D are defined exclusively, e.g. an event fulfilling condition A is not listed as fulfilling condition B as well.

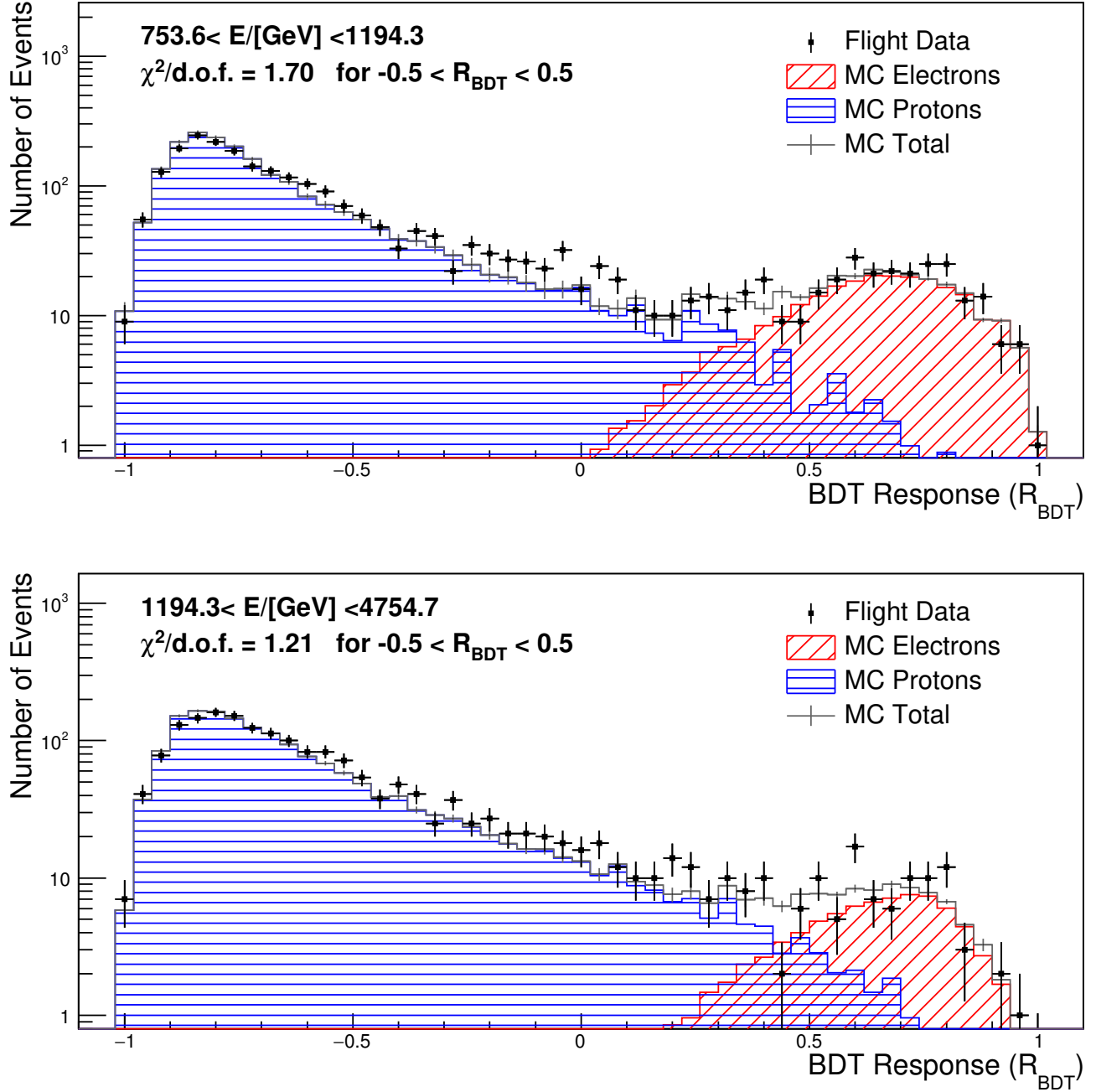


FIG. S2. Examples of BDT response (R_{BDT}) distributions in the $754 < E < 1194$ GeV (*Top*) and $1194 < E < 4575$ GeV (*Bottom*) bins including all acceptance conditions A, B, C and D. While there is noticeable discrepancies in the $-0.3 < R_{\text{BDT}} < 0$ region, their possible effects to the resultant spectrum are included in the systematic uncertainty concerning the BDT stability.

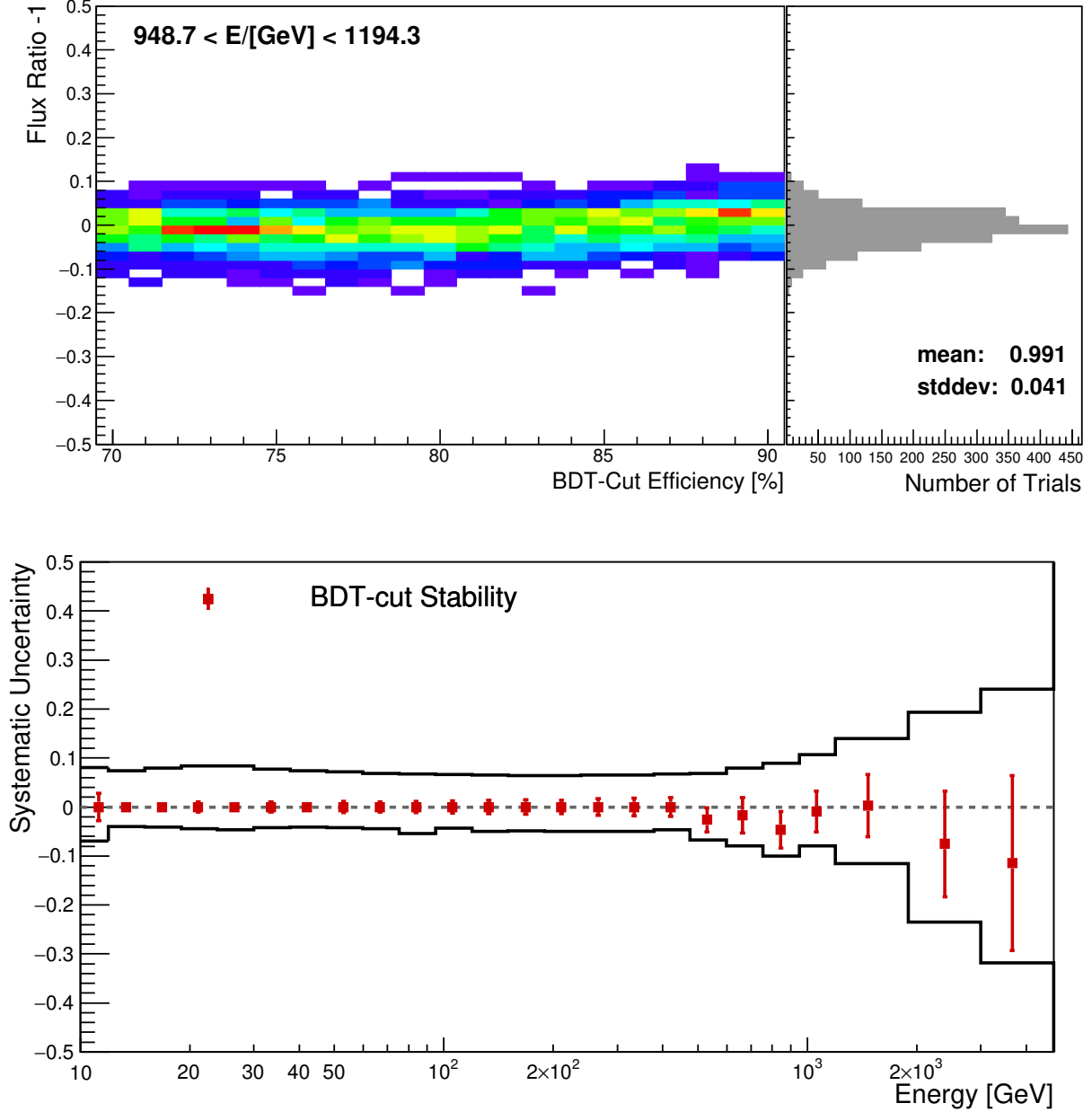


FIG. S3. (Top) Stability of BDT analysis with respect to independent training samples and BDT-cut efficiency in the $949 < E < 1194$ GeV bin. Color maps show the flux ratio dependence on efficiency, where the bin value (number of trials) increases as color changes from violet, blue, green, yellow to red. A projection onto the Y-axis is shown as a rotated histogram (in gray color). (Bottom) Energy dependence of systematic uncertainties. The red squares represent the systematic uncertainties stemming from the electron identification based on BDT. The bands defined by black lines show the sum in quadrature of all the sources of systematics, except the energy scale uncertainties.

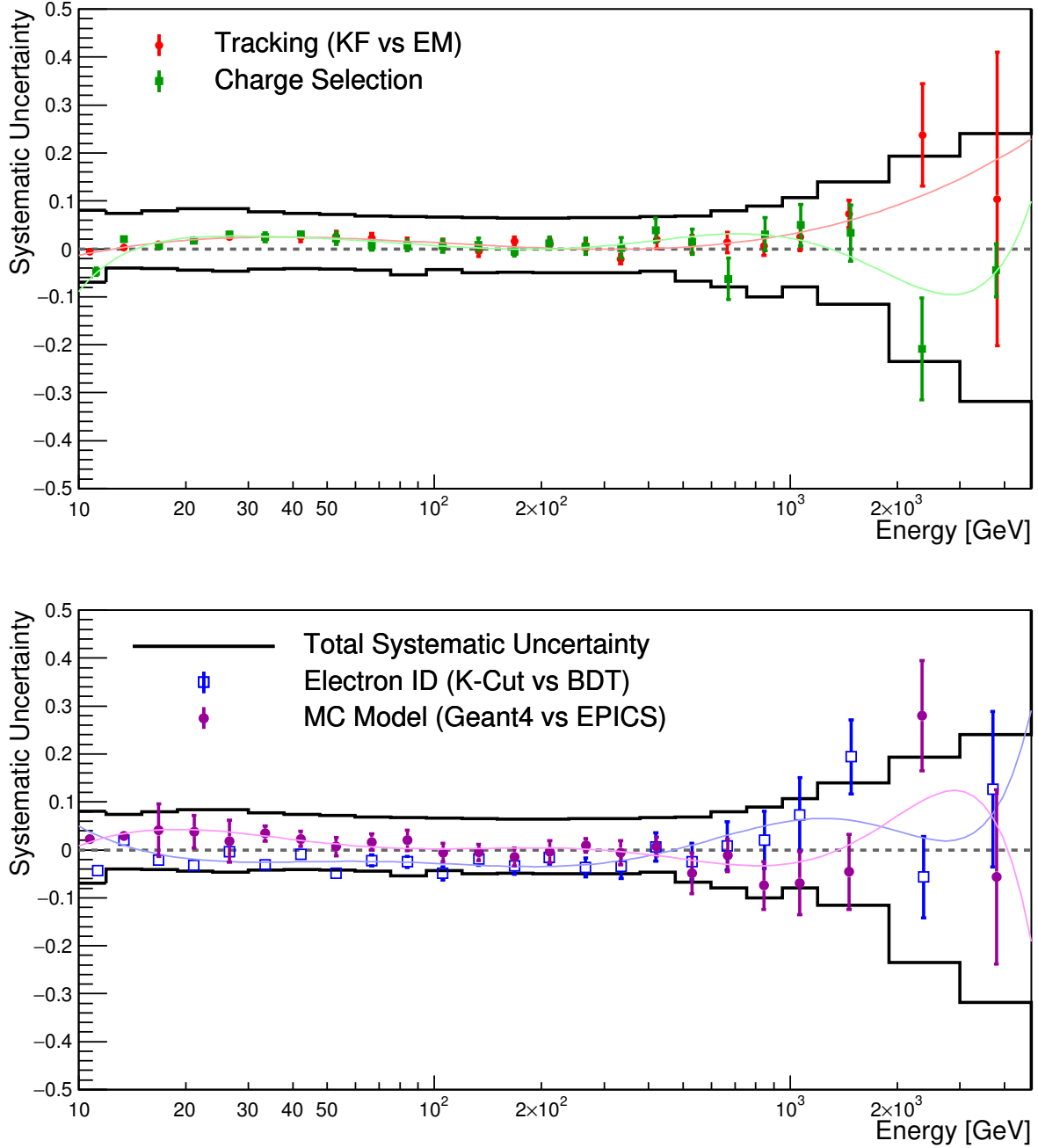


FIG. S4. (*Top*) Energy dependence of systematic uncertainties in tracking algorithms (Electromagnetic shower tracking vs combinatorial Kalman filter tracking) and charge identification methods (CHD vs IMC), (*Bottom*) Energy dependence of systematic uncertainties in electron identification methods (K-estimator vs BDT) and MC models (Geant4 vs EPICS). The data points are fitted with log-polynomial functions to mitigate the effect of statistical fluctuations while preserving possible energy dependent structures. Fit functions are shown as curves and are used to estimate energy dependent systematic uncertainties.

TABLE I. Table of CALET electron plus positron spectrum. Mean energy is calculated using the candidate events in the energy bin. For the flux the first and second errors represent the statistical uncertainties (68% confidence level) and systematic uncertainties, respectively, while uncertainty in the energy scale is not included. Detailed breakdown of systematic errors is included where σ_{BDT} , $\sigma_{\text{trig.}}$, $\Delta_{\text{norm.}}$, $\Delta_{\text{trk.}}$, $\Delta_{\text{chg.}}$, Δ_{ID} and Δ_{MC} denote systematic errors due to BDT stability, trigger, absolute normalization, tracking, charge identification, electron identification, and MC model dependence, respectively. While the first two components must be added in quadrature to the statistical errors in the spectral analysis, the latter five contributions could be treated as nuisance parameters, by introducing correction factors corresponding to each component. Energy dependence (or non-dependence) of each contribution is already determined, constraining the possible corrections due to the nuisance parameters. Although $\Delta_{\text{norm.}}$ can be ignored in a spectral study only using CALET data, it should also be treated as a nuisance parameter in a combined analysis with the positron spectrum, for example.

Energy Bin (GeV)	Mean Energy (GeV)	Flux		Systematic Uncertainties (relative to flux)						
		($\text{m}^{-2}\text{sr}^{-1}\text{s}^{-1}\text{GeV}^{-1}$)		σ_{BDT}	$\sigma_{\text{trig.}}$	$\Delta_{\text{norm.}}$	$\Delta_{\text{trk.}}$	$\Delta_{\text{chg.}}$	Δ_{ID}	Δ_{MC}
10.6–11.9	11.3	$(1.543 \pm 0.004^{+0.094}_{-0.106}) \times 10^{-1}$		0.028	0.024	0.032	-0.006	-0.048	0.031	0.021
11.9–13.4	12.6	$(1.065 \pm 0.003^{+0.057}_{-0.049}) \times 10^{-1}$		0.010	0.024	0.032	0.000	-0.021	0.016	0.030
13.4–15.0	14.2	$(7.388 \pm 0.023^{+0.410}_{-0.305}) \times 10^{-2}$		0.010	0.024	0.032	0.006	-0.003	0.004	0.037
15.0–16.9	15.9	$(5.073 \pm 0.018^{+0.302}_{-0.211}) \times 10^{-2}$		0.010	0.024	0.032	0.011	0.010	-0.005	0.041
16.9–18.9	17.8	$(3.521 \pm 0.014^{+0.223}_{-0.152}) \times 10^{-2}$		0.010	0.024	0.032	0.014	0.018	-0.013	0.043
18.9–21.2	20.0	$(2.468 \pm 0.011^{+0.162}_{-0.111}) \times 10^{-2}$		0.010	0.024	0.032	0.018	0.022	-0.018	0.043
21.2–23.8	22.5	$(1.687 \pm 0.008^{+0.112}_{-0.079}) \times 10^{-2}$		0.010	0.024	0.032	0.020	0.025	-0.022	0.041
23.8–26.7	25.2	$(1.171 \pm 0.006^{+0.077}_{-0.055}) \times 10^{-2}$		0.008	0.024	0.032	0.022	0.026	-0.024	0.038
26.7–30.0	28.3	$(8.029 \pm 0.034^{+0.516}_{-0.385}) \times 10^{-3}$		0.008	0.024	0.032	0.023	0.026	-0.025	0.035
30.0–33.7	31.7	$(5.413 \pm 0.026^{+0.313}_{-0.229}) \times 10^{-3}$		0.011	0.000	0.032	0.024	0.026	-0.026	0.031
33.7–37.8	35.6	$(3.721 \pm 0.020^{+0.206}_{-0.157}) \times 10^{-3}$		0.011	0.000	0.032	0.025	0.025	-0.026	0.026
37.8–42.4	39.9	$(2.612 \pm 0.016^{+0.137}_{-0.109}) \times 10^{-3}$		0.010	0.000	0.032	0.024	0.024	-0.025	0.022
42.4–47.5	44.8	$(1.798 \pm 0.013^{+0.090}_{-0.075}) \times 10^{-3}$		0.010	0.000	0.032	0.024	0.023	-0.025	0.018
47.5–53.3	50.3	$(1.255 \pm 0.010^{+0.060}_{-0.052}) \times 10^{-3}$		0.011	0.000	0.032	0.023	0.021	-0.024	0.014
53.3–59.9	56.4	$(8.863 \pm 0.078^{+0.404}_{-0.367}) \times 10^{-4}$		0.011	0.000	0.032	0.022	0.019	-0.024	0.010
59.9–67.2	63.3	$(6.157 \pm 0.061^{+0.266}_{-0.254}) \times 10^{-4}$		0.010	0.000	0.032	0.020	0.017	-0.024	0.007
67.2–75.4	71.0	$(4.188 \pm 0.048^{+0.173}_{-0.174}) \times 10^{-4}$		0.010	0.000	0.032	0.019	0.015	-0.025	0.005
75.4–84.6	79.7	$(2.984 \pm 0.038^{+0.119}_{-0.126}) \times 10^{-4}$		0.012	0.000	0.032	0.017	0.012	-0.025	0.003
84.6–94.9	89.4	$(2.032 \pm 0.030^{+0.078}_{-0.087}) \times 10^{-4}$		0.012	0.000	0.032	0.015	0.010	-0.027	0.002
94.9–106.4	100.4	$(1.45 \pm 0.02^{+0.05}_{-0.06}) \times 10^{-4}$		0.013	0.000	0.032	0.013	0.007	-0.028	0.002
106.4–119.4	112.6	$(9.82 \pm 0.18^{+0.36}_{-0.45}) \times 10^{-5}$		0.013	0.000	0.032	0.011	0.005	-0.030	0.002
119.4–134.0	126.2	$(6.98 \pm 0.15^{+0.25}_{-0.33}) \times 10^{-5}$		0.014	0.000	0.032	0.009	0.003	-0.031	0.003
134.0–150.4	141.7	$(4.93 \pm 0.12^{+0.18}_{-0.24}) \times 10^{-5}$		0.014	0.000	0.032	0.007	0.001	-0.033	0.003
150.4–168.7	159.0	$(3.47 \pm 0.09^{+0.12}_{-0.17}) \times 10^{-5}$		0.014	0.000	0.032	0.005	-0.000	-0.034	0.004
168.7–189.3	178.8	$(2.48 \pm 0.07^{+0.09}_{-0.12}) \times 10^{-5}$		0.014	0.000	0.032	0.003	-0.001	-0.035	0.004
189.3–212.4	200.1	$(1.69 \pm 0.06^{+0.06}_{-0.08}) \times 10^{-5}$		0.014	0.000	0.032	0.002	-0.001	-0.035	0.004
212.4–238.3	224.4	$(1.20 \pm 0.04^{+0.04}_{-0.06}) \times 10^{-5}$		0.014	0.000	0.032	0.001	0.000	-0.034	0.004
238.3–267.4	252.5	$(8.06 \pm 0.35^{+0.29}_{-0.39}) \times 10^{-6}$		0.017	0.000	0.032	-0.000	0.002	-0.032	0.003
267.4–300.0	282.9	$(5.88 \pm 0.28^{+0.21}_{-0.27}) \times 10^{-6}$		0.017	0.000	0.032	-0.001	0.005	-0.029	0.001
300.0–336.6	317.4	$(4.05 \pm 0.22^{+0.15}_{-0.18}) \times 10^{-6}$		0.018	0.000	0.032	-0.001	0.008	-0.025	-0.002
336.6–377.7	355.6	$(2.73 \pm 0.17^{+0.10}_{-0.11}) \times 10^{-6}$		0.018	0.000	0.032	-0.000	0.012	-0.019	-0.005
377.7–423.8	400.4	$(1.74 \pm 0.13^{+0.07}_{-0.07}) \times 10^{-6}$		0.019	0.000	0.032	0.000	0.016	-0.012	-0.010
423.8–475.5	447.7	$(1.19 \pm 0.10^{+0.05}_{-0.05}) \times 10^{-6}$		0.019	0.000	0.032	0.002	0.020	-0.004	-0.014
475.5–598.6	529.3	$(6.90 \pm 0.40^{+0.29}_{-0.44}) \times 10^{-7}$		$^{+0.000}_{-0.051}$	0.000	0.032	0.005	0.026	0.010	-0.021
598.6–753.6	666.3	$(3.27 \pm 0.25^{+0.19}_{-0.22}) \times 10^{-7}$		$^{+0.019}_{-0.053}$	0.000	0.032	0.011	0.031	0.030	-0.030
753.6–948.7	843.7	$(1.74 \pm 0.16^{+0.12}_{-0.17}) \times 10^{-7}$		$^{+0.000}_{-0.083}$	0.000	0.032	0.021	0.029	0.050	-0.033
948.7–1194.3	1063.6	$(8.84 \pm 1.02^{+0.77}_{-0.57}) \times 10^{-8}$		$^{+0.032}_{-0.051}$	0.000	0.032	0.035	0.018	0.063	-0.025
1194.3–1892.9	1463.2	$(2.04 \pm 0.30^{+0.23}_{-0.14}) \times 10^{-8}$		$^{+0.066}_{-0.061}$	0.000	0.032	0.059	-0.015	0.062	0.010
1892.9–3000.0	2336.2	$(4.19 \pm 1.14^{+0.67}_{-0.85}) \times 10^{-9}$		$^{+0.032}_{-0.183}$	0.000	0.032	0.110	-0.083	0.026	0.102
3000.0–4754.7	3815.3	$(9.36^{+5.37+2.11}_{-4.47-2.79}) \times 10^{-10}$		$^{+0.064}_{-0.293}$	0.000	0.032	0.187	-0.045	0.090	0.051

TABLE II. Table of CALET electron plus positron spectrum using the same energy binning as the DAMPE spectrum. The tabulated information is the same as the previous table.

Energy Bin (GeV)	Mean Energy (GeV)	Flux		Systematic Uncertainties (relative to flux)					
		($\text{m}^{-2}\text{sr}^{-1}\text{s}^{-1}\text{GeV}^{-1}$)	σ_{BDT}	$\sigma_{\text{trig.}}$	$\Delta_{\text{norm.}}$	$\Delta_{\text{trk.}}$	$\Delta_{\text{chg.}}$	Δ_{ID}	Δ_{MC}
10.6–12.2	11.4	$(1.526 \pm 0.004_{-0.103}^{+0.093}) \times 10^{-1}$	0.028	0.024	0.032	-0.006	-0.046	0.030	0.022
12.2–13.9	13.0	$(9.930 \pm 0.027_{-0.439}^{+0.533}) \times 10^{-2}$	0.010	0.024	0.032	0.002	-0.016	0.013	0.032
13.9–16.0	14.9	$(6.277 \pm 0.019_{-0.258}^{+0.358}) \times 10^{-2}$	0.010	0.024	0.032	0.008	0.003	-0.000	0.039
16.0–18.3	17.0	$(4.028 \pm 0.014_{-0.171}^{+0.250}) \times 10^{-2}$	0.010	0.024	0.032	0.013	0.015	-0.010	0.042
18.3–20.9	19.5	$(2.650 \pm 0.010_{-0.118}^{+0.173}) \times 10^{-2}$	0.010	0.024	0.032	0.017	0.022	-0.017	0.043
20.9–24.0	22.4	$(1.701 \pm 0.008_{-0.079}^{+0.113}) \times 10^{-2}$	0.010	0.024	0.032	0.020	0.025	-0.022	0.041
24.0–27.5	25.6	$(1.114 \pm 0.006_{-0.053}^{+0.073}) \times 10^{-2}$	0.008	0.024	0.032	0.022	0.026	-0.024	0.038
27.5–31.6	29.4	$(7.059 \pm 0.028_{-0.339}^{+0.449}) \times 10^{-3}$	0.008	0.024	0.032	0.024	0.026	-0.025	0.034
31.6–36.3	33.8	$(4.399 \pm 0.021_{-0.186}^{+0.249}) \times 10^{-3}$	0.011	0.000	0.032	0.024	0.026	-0.026	0.028
36.3–41.7	38.8	$(2.854 \pm 0.016_{-0.119}^{+0.152}) \times 10^{-3}$	0.010	0.000	0.032	0.024	0.024	-0.025	0.023
41.7–47.9	44.6	$(1.818 \pm 0.012_{-0.075}^{+0.091}) \times 10^{-3}$	0.010	0.000	0.032	0.024	0.023	-0.025	0.018
47.9–55.0	51.2	$(1.182 \pm 0.009_{-0.049}^{+0.056}) \times 10^{-3}$	0.011	0.000	0.032	0.023	0.021	-0.024	0.013
55.0–63.1	58.7	$(7.670 \pm 0.066_{-0.318}^{+0.344}) \times 10^{-4}$	0.011	0.000	0.032	0.021	0.018	-0.024	0.009
63.1–72.4	67.4	$(4.988 \pm 0.049_{-0.206}^{+0.210}) \times 10^{-4}$	0.010	0.000	0.032	0.019	0.016	-0.024	0.006
72.4–83.2	77.5	$(3.191 \pm 0.036_{-0.135}^{+0.128}) \times 10^{-4}$	0.012	0.000	0.032	0.017	0.013	-0.025	0.004
83.2–95.5	88.8	$(2.072 \pm 0.027_{-0.089}^{+0.080}) \times 10^{-4}$	0.012	0.000	0.032	0.015	0.010	-0.026	0.002
95.5–109.7	102.0	$(1.36 \pm 0.02_{-0.06}^{+0.05}) \times 10^{-4}$	0.013	0.000	0.032	0.012	0.007	-0.028	0.002
109.7–125.9	117.2	$(8.81 \pm 0.15_{-0.40}^{+0.32}) \times 10^{-5}$	0.013	0.000	0.032	0.010	0.004	-0.030	0.002
125.9–144.5	134.5	$(5.73 \pm 0.12_{-0.27}^{+0.20}) \times 10^{-5}$	0.014	0.000	0.032	0.008	0.002	-0.032	0.003
144.5–166.0	154.3	$(3.80 \pm 0.09_{-0.19}^{+0.14}) \times 10^{-5}$	0.014	0.000	0.032	0.005	-0.000	-0.034	0.004
166.0–190.6	177.6	$(2.54 \pm 0.07_{-0.13}^{+0.09}) \times 10^{-5}$	0.014	0.000	0.032	0.003	-0.001	-0.035	0.004
190.6–218.8	203.7	$(1.63 \pm 0.05_{-0.08}^{+0.06}) \times 10^{-5}$	0.014	0.000	0.032	0.002	-0.001	-0.035	0.004
218.8–251.2	233.7	$(1.03 \pm 0.04_{-0.05}^{+0.04}) \times 10^{-5}$	0.014	0.000	0.032	0.000	0.001	-0.034	0.003
251.2–288.4	268.5	$(6.88 \pm 0.28_{-0.33}^{+0.25}) \times 10^{-6}$	0.017	0.000	0.032	-0.001	0.003	-0.031	0.002
288.4–331.1	308.2	$(4.51 \pm 0.21_{-0.20}^{+0.17}) \times 10^{-6}$	0.018	0.000	0.032	-0.001	0.007	-0.026	-0.001
331.1–380.2	353.3	$(2.85 \pm 0.16_{-0.12}^{+0.11}) \times 10^{-6}$	0.018	0.000	0.032	-0.000	0.011	-0.020	-0.005
380.2–436.5	407.5	$(1.72 \pm 0.11_{-0.07}^{+0.07}) \times 10^{-6}$	0.019	0.000	0.032	0.001	0.017	-0.011	-0.010
436.5–501.2	466.5	$(1.12 \pm 0.07_{-0.05}^{+0.05}) \times 10^{-6}$	0.019	0.000	0.032	0.002	0.022	-0.001	-0.016
501.2–575.4	536.5	$(6.50 \pm 0.50_{-0.42}^{+0.28}) \times 10^{-7}$	$^{+0.000}_{-0.051}$	0.000	0.032	0.005	0.026	0.011	-0.022
575.4–660.7	615.3	$(4.49 \pm 0.38_{-0.30}^{+0.24}) \times 10^{-7}$	$^{+0.019}_{-0.053}$	0.000	0.032	0.009	0.030	0.023	-0.027
660.7–758.6	708.9	$(2.58 \pm 0.28_{-0.18}^{+0.16}) \times 10^{-7}$	$^{+0.019}_{-0.053}$	0.000	0.032	0.014	0.031	0.036	-0.032
758.6–871.0	809.7	$(1.87 \pm 0.22_{-0.18}^{+0.13}) \times 10^{-7}$	$^{+0.000}_{-0.083}$	0.000	0.032	0.019	0.030	0.047	-0.033
871.0–1000.0	929.9	$(1.38 \pm 0.18_{-0.13}^{+0.10}) \times 10^{-7}$	$^{+0.000}_{-0.083}$	0.000	0.032	0.026	0.026	0.056	-0.031
1000.0–1148.2	1080.5	$(9.31 \pm 1.35_{-0.60}^{+0.81}) \times 10^{-8}$	$^{+0.032}_{-0.051}$	0.000	0.032	0.036	0.017	0.063	-0.024
1148.2–1318.3	1224.8	$(4.48 \pm 0.89_{-0.27}^{+0.41}) \times 10^{-8}$	$^{+0.032}_{-0.051}$	0.000	0.032	0.044	0.006	0.065	-0.013
1318.3–1513.6	1400.8	$(1.67 \pm 0.52_{-0.12}^{+0.19}) \times 10^{-8}$	$^{+0.066}_{-0.061}$	0.000	0.032	0.055	-0.009	0.064	0.004
1513.6–1737.8	1618.3	$(1.88 \pm 0.52_{-0.14}^{+0.22}) \times 10^{-8}$	$^{+0.066}_{-0.061}$	0.000	0.032	0.069	-0.030	0.057	0.028
1737.8–1995.3	1891.3	$(1.25 \pm 0.39_{-0.11}^{+0.17}) \times 10^{-8}$	$^{+0.066}_{-0.061}$	0.000	0.032	0.085	-0.053	0.045	0.059
1995.3–2290.9	2162.0	$(3.79_{-2.04}^{+3.08} \pm 0.55) \times 10^{-9}$	$^{+0.032}_{-0.183}$	0.000	0.032	0.100	-0.073	0.032	0.087
2290.9–2630.3	2481.2	$(3.06_{-1.37}^{+2.29} \pm 0.52) \times 10^{-9}$	$^{+0.032}_{-0.183}$	0.000	0.032	0.118	-0.089	0.022	0.111
2630.3–3019.9	2873.3	$(3.13_{-1.63}^{+2.04} \pm 0.60) \times 10^{-9}$	$^{+0.032}_{-0.183}$	0.000	0.032	0.140	-0.096	0.020	0.124
3019.9–3467.4	3133.1	$(1.05_{-0.71}^{+1.43} \pm 0.22) \times 10^{-9}$	$^{+0.064}_{-0.293}$	0.000	0.032	0.153	-0.091	0.027	0.119
3467.4–3981.1	3738.3	$(9.60_{-6.45}^{+12.67} \pm 2.12) \times 10^{-10}$	$^{+0.064}_{-0.293}$	0.000	0.032	0.183	-0.053	0.079	0.063
3981.1–4570.9	4170.3	$(8.29_{-5.60}^{+11.21} \pm 2.17) \times 10^{-10}$	$^{+0.064}_{-0.293}$	0.000	0.032	0.203	-0.002	0.149	-0.020

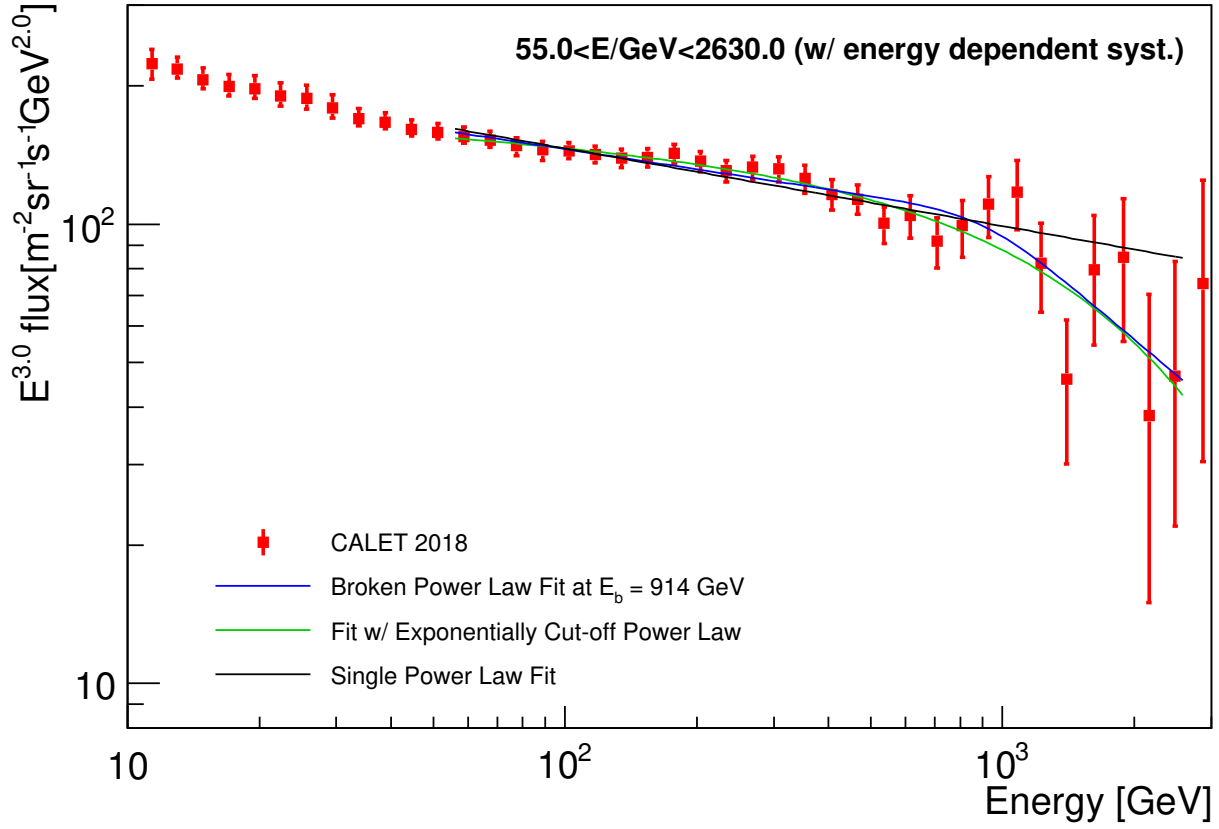


FIG. S5. The fit of the CALET all-electron spectrum with a smoothly broken power law model [S1] (blue line), while fixing the break energy at 914 GeV as determined by DAMPE [S1]. The smoothly broken power law model is defined as: $\Phi(E) = \Phi_0 (E/100 \text{ GeV})^{-\gamma_1} [1 + (E/E_b)^{-(\gamma_1 - \gamma_2)/\Delta}]^{-\Delta}$, where E_b is the break energy, while γ_1 and γ_2 are the power law indices below and above the break energy, respectively. The smoothness parameter, Δ , is fixed to 0.1. The fitting yields $\gamma_1 = -3.15 \pm 0.02$ and $\gamma_2 = -3.81 \pm 0.32$ with a χ^2 of 17.0 and number of degree of freedom (NDF) being 25. If we fit the spectrum with an exponentially cut-off power law [S2] (green line), we obtain 2.3 ± 0.7 TeV as the cutoff energy and a spectral index of -3.06 ± 0.03 with $\chi^2/NDF = 13.0/25$. On the other hand, a single power law fit (black line) in the same energy range gives an index of -3.17 ± 0.02 with $\chi^2/NDF = 26.5/26$. All the parameters are consistent within errors between this energy binning (as shown in Table II) and our original energy binning (as shown in Table I).

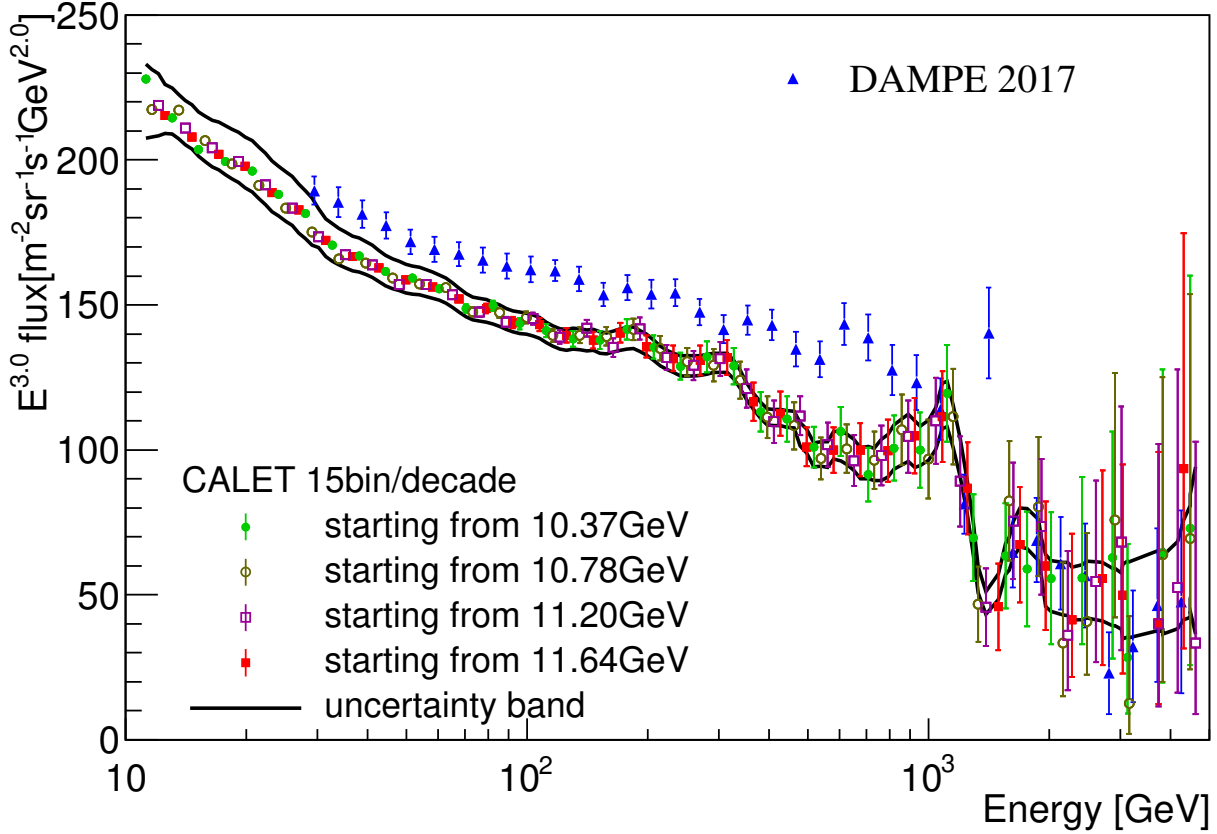


FIG. S6. Study of possible binning related effects in the CALET electron and positron spectrum. To further test the presence of potential systematics in our spectrum, different choices for the adopted binning are checked where the bin-width is chosen as 15 bins/decade in equal log-bins and four different binnings are shown in the same plot. Each binning is shifted by one fourth of the bin width to study possible binning related issues. The solid curves in the figure show the energy dependent systematic uncertainty band. Transition from event selection A+B with K-cut to A+B+C+D acceptance with BDT occurs in both cases at the low-edge of the bin containing 500 GeV. As demonstrated, the deviation due to binning is well below our energy dependent systematic uncertainty or statistical fluctuations. Therefore, bin-to-bin migration and related effects are negligible compared to our estimated systematic uncertainties, in accordance with the estimated CALET energy resolution of 2% above 20 GeV.

* yoichi.asaoka@aoni.waseda.jp

† torii.shoji@waseda.jp

[S1] G. Ambrosi *et al.*, Nature **552**, 63 (2017).

[S2] S. Abdollahi *et al.*, Phys. Rev. D **95**, 082007 (2017).